Inorganic Chemistry

pubs.acs.org/IC Article

Role of the Eu^{3+} Distribution on the Properties of β-$Ca_3(PO_4)_2$ Phosphors: Structural, Luminescent, and ^{151}Eu Mössbauer Spectroscopy Study of $Ca_{9.5-1.5x}MgEu_x(PO_4)_7$

Dina V. Deyneko,* Dmitry A. Spassky, Vladimir A. Morozov, Sergey M. Aksenov, Stanislav P. Kubrin, Maxim S. Molokeev, and Bogdan I. Lazoryak

Cite This: *Inorg. Chem.* 2021, 60, 3961−3971 Read Online

ACCESS | Metrics & More | Article Recommendations | Supporting Information

ABSTRACT: The series of β-$Ca_3(PO_4)_2$-type phosphors $Ca_{9.5-1.5x}MgEu_x(PO_4)_7$ were synthesized by a solid-state route. Observation of the proper Eu^{3+} ion distribution in the $Ca_{9.5}Mg(PO_4)_7$ host matrix was made by a direct method using ^{151}Eu Mössbauer spectroscopy in combination with X-ray analysis and dielectric and luminescent spectroscopy. The photoluminescence properties were studied in detail. The samples exhibit an exceptionally narrow-band red emission according to the dominant $^5D_0 \rightarrow {}^7F_2$ transition and fulfill the industrial requirements for high-energy-efficiency red phosphors. The contribution of Eu^{3+} ions in different crystal sites to the luminescent properties is discussed in detail. The difference of the excitation of Eu^{3+} in the M1 and M2 sites was revealed by photoluminescence excitation spectra in accordance with structure refinement. The temperature dependence of the luminescence intensity was studied. Different tendencies in the thermal behavior of emission lines allow one to consider the studied compounds as phosphors suitable for luminescence thermometry. The measured quantum yield for $Ca_{9.5-1.5x}MgEu_x(PO_4)_7$ shows excellent results and reaches 63%.

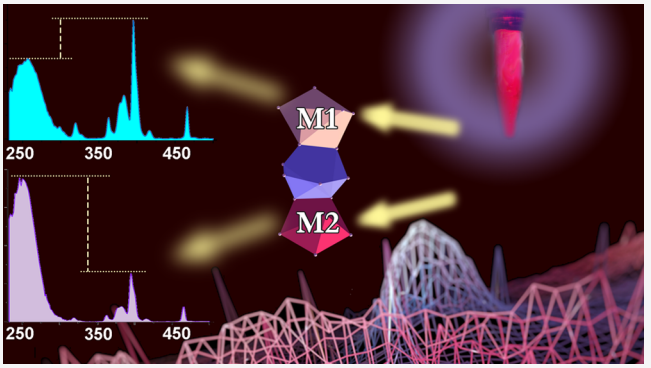

INTRODUCTION

Advances in solid-state lighting[1] lead to the development of new types of inorganic/organic/hybrid phosphors.[2,3] In particular, a considerable part of world energy consumption is represented by outdoor lighting,[4] which uses almost only inorganic phosphors.[1] Therefore, phosphors for commercial application should meet the following requirements: excellent chemical homogeneity and thermal stability, durability, and isotropy of the optical properties. However, even the presence of the whole set of above-mentioned requirements does not provide a sufficient guarantee that the obtained phosphor would be cheap and simple to produce. In this case, it is necessary to use a well-known material with outstanding physical and chemical properties as an initial matrix to design and develop new types of phosphors.[3,5,6] Compounds with the β-$Ca_3(PO_4)_2$-type (or β-TCP) structure and different chemical compositions have been synthesized and studied as novel and prospective inorganic phosphors.[7,8] Because of the wide isomorphous capacity (which allows tailoring of the optical features)[9−12] represented by different homo- and heterovalent cationic substitutions, these phosphors have several advantages for application in light-emitting-diode (LED) technology and can be considered as a good base to form a popular branch in luminescence research.

An appropriate combination of inorganic host material with the different luminescent rare-earth (RE) ions as dopants is the mainstream essence of phosphor-converted LEDs (pc-LEDs). The host matrix strongly effects the luminescence properties of activator ions.[13] For example, the starting β-TCP-type (TCP = tricalcium phosphate) host[14] does not show bright luminesce directly if there are no dopant luminescent ions; however, the insertion of lanthanide elements into the initial matrix can produce a visible light through their electron transitions in the 4f shell.[15] Because of the shielding of 4f electrons by 5s and 5p electrons, the radiative transitions of trivalent RE ions are represented by narrow and intense bands. The narrow-band emission is an industrial requirement for high-performance pc-LED devices.[16] The luminous efficacy is maximum when the emission band width is less than 20 nm.[16] Numerous isostructural β-TCP-type phosphors with different combinations of cations and anions have been synthesized to produce

Received: December 29, 2020
Published: March 1, 2021

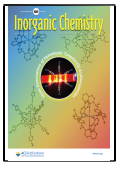

https://dx.doi.org/10.1021/acs.inorgchem.0c03813
Inorg. Chem. 2021, 60, 3961−3971

the brightest one. A number of Eu^{3+}-doped materials have been studied to develop the red-emitting phosphors for pc-LEDs. The 4f−4f transitions of Eu^{3+}-doped phosphors can overlap with near-UV LED chip radiation, UV-emitting InGaN, for instance. However, these transitions with low oscillator strengths ($<10^6$) are forbidden, so the absorption of near-UV radiation by Eu^{3+} ions is weak.

The β-TCP-type phosphors doped by Eu^{3+} ions are well-known because of their strong luminescence in the red spectral region. Due to the environmentally sensitive 4f transitions of Eu^{3+} ions,[17] deliberate cationic substitution can be an effective strategy for achieving efficient luminescence. The Eu^{3+} emission in β-TCP-type phosphors meets the requirement of narrow-band red emission because the most intensive radiative transition $^5D_0 \rightarrow {}^7F_2$ is relatively narrow.[15] The wide red emission of the phosphor causes a significant spillover of light into the deeper red spectral area, where the human eye is less sensitive, and leads to the spectral inefficiency of the pc-LED device.[16]

The distribution of Eu^{3+} ions between different crystallographic sites of the β-TCP-type structure plays a key role because the luminescence intensity is very sensitive and depends on the local symmetry and coordination environment (in particular, different bond-length distances and distortion of the polyhedra) of the dopant RE ions.[18] The local states of Eu^{3+} ions influence the intensity and some distinguished features of the resulting spectra because some transitions can be forbidden due to selection rules. The radiative transitions of Eu^{3+} ions in this host are allowed because of the features of the β-TCP-type structure.[19] In this case, systematical and fundamental investigation is necessary to reveal the relationship between the symmetry of the host lattice, distribution of Eu^{3+} activators, and observed emission.

The correct determination of the structure is important for further application of these phosphors in pc-LED technology. Unfortunately, such a distribution of the dopant activator ions has not been studied directly using the fine spectroscopic methods so far. In most of studies of phosphors with β-TCP-type structure, the real distribution of Eu^{3+} ions remains unknown, and the conclusion is based on refinement of the crystal structures. However, such an approach is limited by the quality of the crystals and depends on accurate analysis of the mixture composition within the crystallographic sites.

In this paper, we provide direct observation of the Eu^{3+} ion distribution in the $Ca_{9.5}Mg(PO_4)_7$ host matrix with the β-TCP-type structure by a direct method using ^{151}Eu Mössbauer spectroscopy in combination with X-ray analysis and dielectric and luminescent spectroscopy to understand the role of such distribution in the luminescent properties. This gives us a opportunity to reveal the influence of the coordination environment of Eu^{3+} ions in the β-TCP-type structure on the optical properties of these compounds.

EXPERIMENTAL SECTION

Materials and Sample Preparation. Phosphates $Ca_{9.5-1.5x}MgEu_x(PO_4)_7$ ($0.12 \leq x \leq 1.00$) were synthesized by a high-temperature solid-state reaction from stoichiometric mixtures of $CaHPO_4{\cdot}2H_2O$ (99.9%), $CaCO_3$ (99.9%), MgO (99.99%), and Eu_2O_3 (99.9%) purchased from Sigma-Aldrich. In the first step, the compounds were weighed and ground in an agate mortar by using a small quantity of acetone or ethanol. The mixtures were sintered at 773 K for 5 h with moderate grinding. Then, the samples were transferred to Al_2O_3 crucibles and annealed at 1273 K for 10 h in air. Finally, the products were furnace-cooled to room temperature and ground for subsequent measurements. The powder X-ray diffraction (PXRD) patterns of the prepared compounds were checked using the JCPDS PDF-2 Database, and it did not indicate any reflections of the initial or intermediate phases.

Characterization. Energy-dispersive X-ray (EDX) analysis of $Ca_{9.5-1.5x}MgEu_x(PO_4)_7$ (x = 0.75) was performed using a Titan Themis transmission electron microscope operating at 200 kV with a Super-X detector and an EDAX attachment. Samples for transmission electron microscopy (TEM) were prepared by crushing powders in agate mortars and dispersing them in methanol. After treatment in an ultrasonic bath to disperse crystallites, a few drops of the dispersion were placed on copper grids with a holey carbon film. The EDX analysis results were based on the Mg K-, Ca K-, and Eu L-edge lines. The EDX measurements of the Ca/Mg/Eu ratio were provided for probe diameters of 100−200 nm.

The ^{151}Eu Mössbauer spectra were taken with a MS1104Em spectrometer. The moving-sample geometry was employed. ^{151}Sm was used as a source of γ radiation. All isomer shift values (δ) given hereafter are referred to as Eu_2O_3. Experimental data were resolved as symmetric singlets with equal width at half-maximum (G) and Lorentzian line shapes using *UnivemMS* software.

PXRD patterns were collected at room temperature with a Bruker D8 ADVANCE powder diffractometer (Cu Kα radiation, 40 kV, 40 Ma, Bruker, Billerica, MA) and a linear VANTEC detector. The step size of 2θ was 0.016°, and the counting time was 1 s per step in the 2θ range between 5° and 140°. The Rietveld refinement was applied using *JANA2006* software.[20] Illustrations were created with *JANA2006* and *DIAMOND*.[21]

The second-harmonic-generation (SHG) signal was measured with a Q-switched YAG:Nd laser at λ_ω = 1064 nm in the reflection mode. The experimental setup and arrangement were described previously.[22]

The dielectric permittivity ε and dielectric loss tangent (tan δ) in air were measured by a double-contact method in the frequency range of 1−106 Hz at 300−1270 K (heating rate of 5 K·min^{-1}), with the help of a Solartron 7081 precision voltmeter and a Solartron 1260 frequency response analyzer. Ceramic pellets (1.5 mm thick and 5−6 mm in diameter) were prepared by pressing and sintering at 1473 K for 12 h. Pt paste was put on flat surfaces of the pellets, and then they were heated at 1023 K for 4 h to produce Pt electrodes.

Photoluminescence emission (PL) and excitation (PLE) spectra were recorded on an Agilent Cary Eclipse fluorescence spectrometer with a 75 W Xe light source (pulse length τ = 2 μs, pulse frequency ν = 80 Hz, wavelength resolution = 0.5 nm; Hamamatsu R928 photomultiplier tube). PL spectra measured in the temperature region of 80−500 K were obtained using a Lot-Oriel MS-257 spectrograph equipped with a Marconi CCD detector and a 150 W Xe arc lamp as an excitation source. The powder samples were placed in an optical cryostat (Cryotrade LM-120). The spectral resolution was 0.15 nm. The PL/PLE spectra of all samples were obtained under similar experimental conditions to compare the relative emission intensities and reduce the error. The obtained spectra were corrected for the sensitivity of the spectrometer. The Gauss fit of the PLE spectra was performed on the energy scale after conversion of the spectra from the nanometer scale with account of the λ^2 factor.

The internal quantum efficiency defined as the ratio of the number of emitted photons to the number of photons absorbed was measured on an Edinburgh Instruments FS5 spectrofluorometer equipped with a SC-30 integrating-sphere module and a Hamamatsu R928 photomultiplier tube. All measurements were performed at room temperature and corrected for the sensitivity of the spectrometer.

RESULTS AND DISCUSSION

Elemental Composition and Preliminary Characterization. EDX analysis of the $Ca_{9.5-1.5x}MgEu_x(PO_4)_7$ (x = 0.75) sample was performed at five points of each crystallite. Using TEM−EDX, the Mg/Ca/Eu ratio for the compound was found to be 1.0:8.27 ± 0.91:0.75 ± 0.07 (9.98 ± 0.95 atom % Mg, 82.55 ± 1.13 atom % Ca, and 7.45 ± 0.38 atom % Eu) and did not significantly differ from the expected bulk composition.

https://dx.doi.org/10.1021/acs.inorgchem.0c03813
Inorg. Chem. 2021, 60, 3961−3971

The O and P contents have not been quantified by EDX. The results of EDX analysis are shown in Figure S1.

PXRD Study. The PXRD patterns of $Ca_{9.5-1.5x}MgEu_x(PO_4)_7$ are shown in Figure 1a. The locations

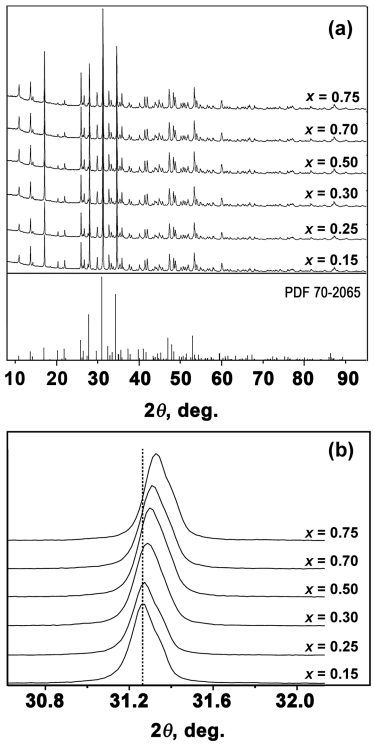

Figure 1. (a) PXRD patterns of $Ca_{9.5-1.5x}MgEu_x(PO_4)_7$ solid solutions and Bragg reflections for β-$Ca_3(PO_4)_2$ (JCPDS PDF-2 70-2065). (b) Shift of the reflections in $Ca_{9.5-1.5x}MgEu_x(PO_4)_7$ solid solutions.

of the diffraction peaks are similar to those of pure β-$Ca_3(PO_4)_2$ (JCPDS PDF-2 70-2065). The PXRD patterns did not contain any impurity phases. The slight shift to larger 2θ angles of the main reflection (0 2 10) was observed in accordance with Bragg's rule (Figure 1b) because the ionic radius of Eu^{3+} at eight coordination is smaller than that of Ca^{2+}. A continuous nature of $Ca^{2+} \rightarrow Eu^{3+}$ substitution in the $Ca_{9.5-1.5x}MgEu_x(PO_4)_7$ solid solutions was also confirmed by calculation of the ratio percentage discrepancy (D_r). The single-phase substitution requires a closeness of the ionic radii between the dopant (R_d) and host (R_h) cations. The ionic radius percentage difference (D_r) should be less than 30%.[23] In this case, the possible sites for Eu^{3+} [r_{VI} = 0.947 and r_{VIII} = 1.066 Å for coordination number (CN) = 6 and 8, respectively] are Ca^{2+} (r_{VIII} = 1.12 Å) and Mg^{2+} (r_{VI} = 0.72 Å).[24] Thus, ionic radius difference could be calculated by the formula

$$D_r = \frac{R_h(CN) - R_d(CN)}{R_h(CN)}$$

where D_r represents the radius percentage discrepancy and CN denotes the coordination number of ions. The results are summarized in Table 1. Thus, the Eu^{3+} ions can continuously substitute the Ca^{2+} ions only in the M1, M2, and M3 sites but not substitute Mg^{2+} ion in the M5 site. The absence of any impurity reflections showed that Eu^{3+} and Mg^{2+} ions were completely incorporated into the β-TCP-type host lattice.

Table 1. Ionic Radius Difference Percentages (D_r) between Host Cations and Doped Eu^{3+} Ions

		D_r, %		
doped ion	radius, Å/CN	Ca^{2+} 1.12 Å/8	Ca^{2+} 1.00 Å/6	Mg^{2+} 0.72 Å/6
Eu^{3+}	1.066 Å/8	4.8		
	0.947 Å/6		5.3	−38.9

SHG Study and Models Tested during the Rietveld Refinement of the Crystal Structure for x = 0.75. A SHG study for $Ca_{9.5-1.5x}MgEu_x(PO_4)_7$ shows a relatively small signal value [$I_{2\omega}/I_{2\omega}(SiO_2) \sim 0$ units from quarts etalon], and it absolutely declines with increasing Eu^{3+} concentration. The SHG data are listed in Table 2. The absence of a signal for the sample with x = 0.75 allows one to suggest a centrosymmetric structure. However, this contradicts the reference data on the structure of β-TCP-related compounds.

The PXRD patterns were used to refine the crystal structure. On the basis of the refined structures of other β-TCP-related compounds, two models have been used for the Rietveld refinement: $R3c$ and $R\bar{3}c$ for the sample with x = 0.75 to ensure SHG.

The β-TCP-type phosphors were characterized by trigonal crystal structures, which can be either polar [space group (SG) $R3c$] or nonpolar (SG $R\bar{3}c$). The general formula, which reflects possible isomorphous substitution (Z = 6), is $Ca_{10.5-0.5(x-2y-3z)}A^+_xB^{2+}_yR^{3+}_z(TO_4)_7$, where A^+ = alkaline cations (Li, Na, K),[11,25−28] B^{2+} = divalent cations (Ca, Mg, Zn, Cd),[29−33] and R^{3+} = trivalent RE elements (Y, Sc, Ln), Bi^{3+}, In^{3+}.[34−36] The β-$Ca_3(PO_4)_2$-type structure consists of five different crystallographic M1−M5 sites: the M1−M3 sites occupy 18b Wyckoff positions and are located at the centers of 8-vertex polyhedra; the M4 site occupies the 6a Wyckoff position and is located at the 3-fold axis at a 15-vertex polyhedron (which is usually half-occupied); the M5 site occupies the 6a Wyckoff position and is also located at the 3-fold axis at the center of a distorted octahedron. In the $R\bar{3}c$ structure, the M1 and M2 sites, $P2O_4$ and $P3O_4$ tetrahedra of the β-TCP-type structure, are equivalent, while the M5, M3 and P1 sites are situated at the center of symmetry. The main difference between the two models is that half of the $P1O_4$ tetrahedra in the $R\bar{3}c$ model are in the opposite orientation compared to the $R3c$ model.

The structural data for β-$Ca_3(PO_4)_2$ (SG $R3c$)[37] and $Ca_8MgEu(PO_4)_7$ (SG $R\bar{3}c$)[19] were used as starting models for the refinement of $Ca_{9.5-1.5x}MgEu_x(PO_4)_7$ (x = 0.75). At the first stage, the f curves for Ca^{2+} (M1−M4 sites) and Mg^{2+} (M5 site) were used, and all parameters of the chosen model were refined. Table S1 lists the results of the Rietveld refinement of the structures in both models. The $R\bar{3}c$ model demonstrates the worst reliability factors, refinement of the structure leads to the P1−O1 distance in the PO_4 tetrahedra, and the isotropic atomic displacement parameter (U_{iso}) for the P1 atom deviated further from the reasonable values than the $R3c$ model. Therefore, the polar SG $R3c$ was chosen.

Refinement of the $Ca_{9.5-1.5x}MgEu_x(PO_4)_7$ Crystal Structures. On the basis of refinement of the crystal structure for x = 0.75, the crystal structures of all $Ca_{9.5-1.5x}MgEu_x(PO_4)_7$ solid solutions were refined in the $R3c$ model.[37] Because of the complex chemical composition, the cation distribution on the structural sites was proposed on the crystal chemical criteria, taking into account site-scattering factors, interatomic

https://dx.doi.org/10.1021/acs.inorgchem.0c03813
Inorg. Chem. 2021, 60, 3961−3971

Table 2. Main Crystallographic Data, SHG Signal, Phase Transition Temperature T_c, and Quantum Yield (QY) for $Ca_{9.5-1.5x}MgEu_x(PO_4)_7$ (T = 293 K, SG $R3c$, Z = 6)

	x = 0.15	x = 0.25	x = 0.3	x = 0.50	x = 0.70	x = 0.75
refined x	0.12	0.22	0.30	0.53	0.67	0.72
SHG	6	2	0.6	0.4	0.2	0
T_c, K	958	938	908	871	851	806
QY, %	61.0	61.2	61.4	62.1	63.0	62.8
a, Å	10.3436(5)	10.3477(1)	10.3514(1)	10.3546(1)	10.3584(6)	10.3610(1)
c, Å	37.1195(3)	37.1323(5)	37.1386(5)	37.1373(4)	37.1281(3)	37.1101(4)
V, Å^3	3439.32(4)	3443.25(7)	3446.31(7)	3448.33(6)	3449.97(4)	3450.05(7)
Data Collection						
diffractometer	Bruker D8 ADVANCE					
radiation/wavelength (λ, Å)	Cu Kα/1.5418					
2θ range, deg	5−140					
step scan (2θ), deg	0.016					
no. of points	8427					
I_{max}	29954	27931	32120	34911	33041	34680
refinement	Rietveld					
background function	Legendre polynomials, 18 terms					
no. of reflns (all/observed)	700/700	761/761	1051/1049	773/771	793/783	781/759
no. of refined param/refined atomic param	74/59	76/55	76/58	77/56	76/56	76/58
R and R_w (%) for Bragg reflections	1.89, 2.26	2.51, 2.77	2.42, 2.75	2.52, 2.71	2.60, 2.75	3.40, 3.54
R_p	3.15	3.01	2.51	2.21	2.08	2.20
R_{wp}	4.12	3.89	3.20	2.85	2.71	2.88
R_{exp}	2.49	2.39	2.08	1.82	1.76	1.70
GOF	1.65	1.62	1.54	1.56	1.54	1.70
max/min residual density	0.24/−0.22	0.29/−0.28	0.35/−0.35	0.40/−0.33	0.43/−0.37	0.59/−0.49
Selected Crystal Structure Data						
e_{calc}(M1)/U_{iso}	20.66/0.014(2)	21.36/0.011(2)	22.34/0.010(2)	22.56/0.008(2)	23.14/0.009(2)	24.26/0.009(2)
e_{calc}(M2)/U_{iso}	20.48/0.011(1)	21.16/0.013(2)	21.42/0.009(1)	21.80/0.008(1)	22.50/0.008(2)	23.10/0.010(2)
e_{calc}(M3)/U_{iso}	20.20/0.011(1)	20.66/0.011(2)	21.26/0.008(1)	21.98/0.011(1)	22.22/0.007(2)	22.92/0.010(2)
e_{calc}(M4)/U_{iso}	8.78/0.020(6)	8.20/0.029(8)	7.30/0.039(9)	5.18/0.05(1)	4.22/0.09(3)	2.98/0.08(3)
CCDC deposition numbers	2052736	2052846	2052848	2052849	2057062	2057061

distances, and ionic radii of the cations. At the first stage, the number of electrons associated with the atoms at the site (e_{calc}) was determined (Table 2). Analysis of the obtained values of e_{calc} showed that the Eu^{3+} ions are located only in the M1−M3 sites. The occupancy of the M4 position by Ca^{2+} decreases with increasing Eu^{3+} concentration during the substitution $Ca^{2+} \rightarrow Eu^{3+}$, and the M4 site[38] becomes vacant (Figure 2). According to the crystal chemical structure, the number of structural units in the cell is Z = 6. So, there are a maximum of six Eu atoms in the structure in the limit composition with x = 1. The number of Eu atoms grows with the $Ca^{2+} \rightarrow Eu^{3+}$ substitution. The comparative distribution of Eu atoms throughout the crystal sites M1−M3 is shown in Figure 3.

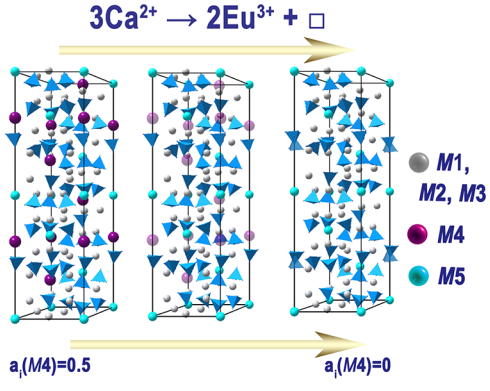

Figure 2. Schematic distribution of ions in the $Ca_{9.5-1.5x}MgEu_x(PO_4)_7$ ($0 \le x \le 1$) solid solutions under $Ca^{2+} \rightarrow Eu^{3+}$ substitution.

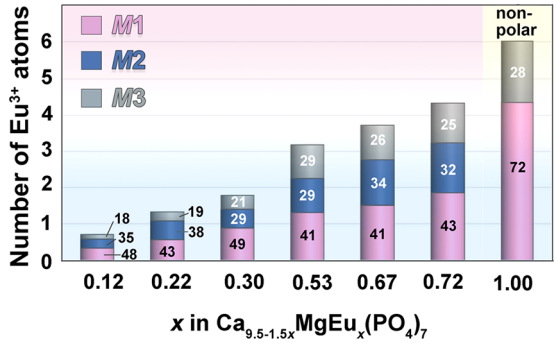

Figure 3. Comparative distribution of Eu^{3+} ions in the crystal sites M1−M3 in $Ca_{9.5-1.5x}MgEu_x(PO_4)_7$. The numerals denote the percentages from all Eu^{3+} atoms in the structure. For x = 1 data from ref 19.

At the second stage, for each value of e_{calc}, the most suitable ratio between the atoms with the closest final refined amount of electrons (e_{ref}) was selected and the atom coordinates and atomic displacement parameters were refined, taking into account their multiplicities (M1−M3) = $n$$Ca^{2+}$ + (1 − n)Eu^{3+} and without stoichiometric constraints on the real Eu/Ca ratio. At the last stage, the occupancy of the M4 position by Ca^{2+} was refined considering the formula neutrality by the equation

https://dx.doi.org/10.1021/acs.inorgchem.0c03813
Inorg. Chem. 2021, 60, 3961−3971

(M4) = 0.5 − 0.5[n_1(Eu1) + n_2(Eu2) + n_3(Eu3)]. Refinement of the distribution of the Eu^{3+} cations over the M1−M3 positions allows us to determine the composition of the $Ca_{9.5-1.5x}MgEu_x(PO_4)_7$ phases (Table 2).

The reliability R factors (Table 2) show a good agreement between the calculated and experimental XRD patterns. For example, Figure 4 displays portions of the observed, calculated,

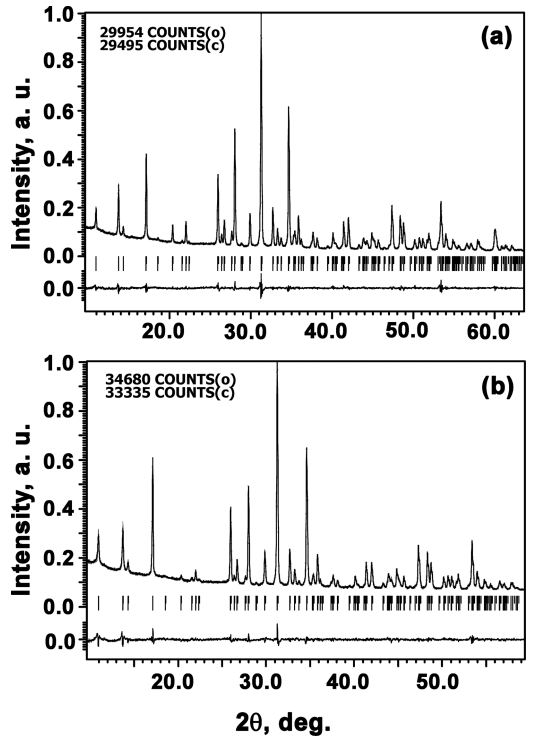

Figure 4. Fragments of the observed, calculated, and difference PXRD patterns for $Ca_{9.5-1.5x}MgEu_x(PO_4)_7$ for x = 0.12 (a) and 0.72 (b). Tick marks denote the peak positions of possible Bragg reflections.

and difference XRD patterns for $Ca_{9.5-1.5x}MgEu_x(PO_4)_7$ for x = 0.12 and 0.72. Other numerical characteristics illustrating the quality of the structure refinements are presented in Table 2. The fractional atomic coordinates, isotropic atomic displacement parameters, cation occupancies, and main relevant interatomic distances for the $Ca_{9.5-1.5x}MgEu_x(PO_4)_7$ phases are listed in Tables S2 and S3. The exact chemical formulas after Rietveld refinement were close to the proper synthesis stoichiometry. The CCDC deposition numbers are 2052736, 2052846, 2052848, 2052849, 2057062, and 2057061.

The symmetry of the averaged crystal field of the ligands created near the M1 and M2 sites is higher than that for the M3 optical center. The average distances M1−O and M2−O reduce with x (Table 3), while M3−O rises. Also, this is confirmed by the polyhedra distortion index (DI) for different CNs calculated as

$$\mathrm{DI} = \frac{1}{n}\sum_{i=1}^{n}\frac{|l_i - l_{av}|}{l_{av}}$$

where n is the coordination number of the central cation, l_i is the distance from the central cation to the O atom, and l_{av} is the average bond length. The data on the DI are given in Table 3. The DI for M3−O rises, while for M1 and M2, it changes slightly.

^{151}Eu Mössbauer Spectroscopy. The experimental Mossbauer spectra are shown in Figure 5. The obtained

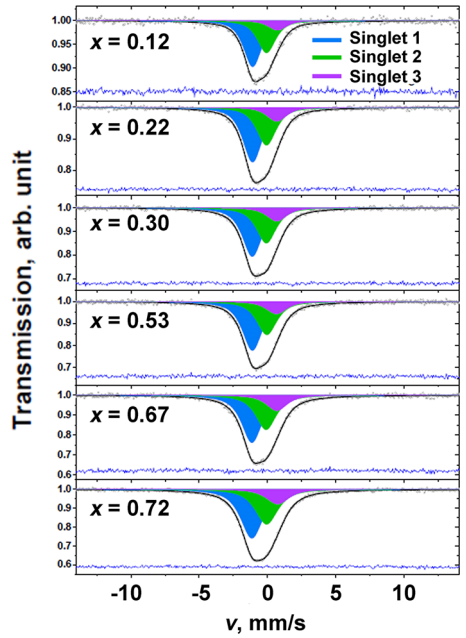

Figure 5. Mössbauer spectroscopy spectra for $Ca_{9.5-1.5x}MgEu_x(PO_4)_7$.

Table 3. Mean Interatomic Distances in the Crystal Structure and Polyhedra DI for $Ca_{9.5-1.5x}MgEu_x(PO_4)_7$

	composition x						
	0.12	0.22	0.30	0.53	0.67	0.72	1.00[a]
M1−O	2.481	2.482	2.480	2.471	2.466	2.474	2.464
DI(M1−O)	0.038	0.041	0.040	0.038	0.035	0.039	0.037
M2−O	2.469	2.461	2.456	2.455	2.455	2.458	
DI(M2−O)	0.038	0.037	0.040	0.038	0.036	0.036	
M3−O	2.511	2.519	2.520	2.531	2.527	2.536	2.829
DI(M3−O)	0.024	0.029	0.028	0.027	0.023	0.046	0.052
M4−O	2.594	2.582	2.621	2.621	2.688	2.743	
Mg−O	2.083	2.100	2.087	2.112	2.114	2.090	2.097
P1−O	1.548	1.575	1.599	1.569	1.571	1.585	1.518
P2−O	1.551	1.554	1.560	1.552	1.553	1.541	1.525
P3−O	1.538	1.531	1.526	1.539	1.545	1.538	

[a]Data from ref 19.

https://dx.doi.org/10.1021/acs.inorgchem.0c03813
Inorg. Chem. 2021, 60, 3961−3971

spectra could be fit by three components with equal width (symmetric singlets), and a slight line broadening from 1.60 to 2.01 was detected. The strongest Singlets 1 (~51%) in all cases with $\delta = -1.09$ to -1.14 mm/s most likely correspond to Eu^{3+} at the M1 site. The additional Singlets 2 (~36%) and weak Singlets 3 (~13%) can be assigned to Eu^{3+} at the M2 and M3 sites, respectively. Such an assignment of the singlets is in good agreement with the X-ray analysis and refinement of the occupancies of Eu^{3+} in the structures (Figure 3 and Table S2) and shows the selective role of the M1 site as the most preferable for RE ions in the β-TCP-type host lattice. For example, the relationship of a_i for the M1/M2/M3 sites is 48%:35%:18% for the sample with $x = 0.12$ according to X-ray data and 52%:37%:11% according to Mössbauer data. Such values are within the instrumental error of the measurement. The Mössbauer parameters and assignments of these singlets are listed in Table 4.

Table 4. Parameters of the ^{151}Eu Mössbauer Spectra of $Ca_{9.5-1.5x}MgEu_x(PO_4)_7$[a]

x	component	$\delta \pm 0.02$, mm/s	$A \pm 1$, %	$G \pm 0.02$, mm/s	Eu^{3+} position	χ^2
0.12	Singlet 1	−1.09	52	1.60	M1	1.089
	Singlet 2	−0.07	37	1.60	M2	
	Singlet 3	0.74	11	1.60	M3	
0.22	Singlet 1	−1.09	51	1.72	M1	1.029
	Singlet 2	−0.08	36	1.72	M2	
	Singlet 3	0.68	13	1.72	M3	
0.29	Singlet 1	−1.12	50	1.75	M1	1.185
	Singlet 2	−0.09	36	1.75	M2	
	Singlet 3	0.68	14	1.75	M3	
0.53	Singlet 1	−1.11	52	1.78	M1	1.055
	Singlet 2	−0.05	35	1.78	M2	
	Singlet 3	0.66	13	1.78	M3	
0.67	Singlet 1	−1.14	49	1.81	M1	1.083
	Singlet 2	−0.11	35	1.81	M2	
	Singlet 3	0.69	16	1.81	M3	
0.72	Singlet 1	−1.14	50	2.01	M1	1.101
	Singlet 2	−0.07	36	2.01	M2	
	Singlet 3	0.75	15	2.01	M3	

[a] δ = isomer shift, A = component area, G = line width, and χ^2 = Pirson's criterion.

Dielectric Measurements. Figure 6a presents the dielectric loss tangent (tan δ) for $Ca_{9.5-1.5x}MgEu_x(PO_4)_7$ phosphates. The maxima were detected for all samples except $x = 1$, so the polar structure (with the noncentrosymmetric SG $R3c$) is attributed to $0 \le x < 1$ in $Ca_{9.5-1.5x}MgEu_x(PO_4)_7$ in accordance with the PXRD data. There are no changes in symmetry, but the effect on the curves becomes smaller and diffused. The sample with $x = 1$ belongs to the nonpolar structure[19,39] (with centrosymmetric SG $R\bar{3}c$), and the absolute absence of the maximum on tan δ was observed (Figure 6a). For $x = 0.72$, the most diffused transition was detected (see the inset in Figure 6a). Such behavior corresponds to cation disordering in the structure (Table 3).

The characteristic maximum on the temperature dependence of the dielectric constant $\varepsilon(T)$ curves was detected (Figure 6b). This peak ($0 \le x < 1$) corresponds to the phase transition at high temperature from a polar (SG $R3c$) to a nonpolar (SG $R\bar{3}c$) structure with ferroelectric type. The rise of ε during heating is due to increasing ionic conductivity.[40]

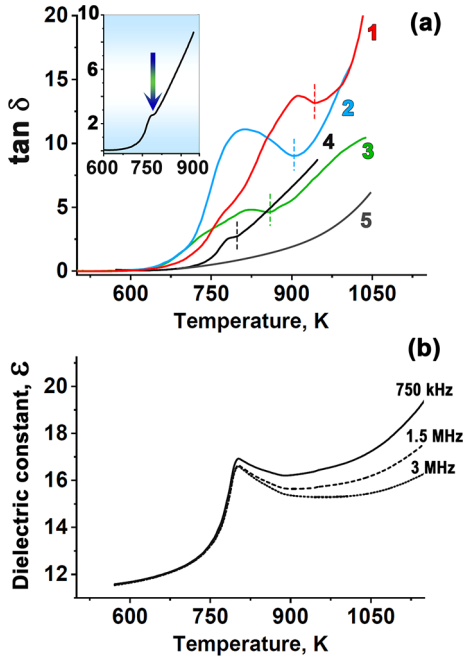

Figure 6. (a) Temperature dependencies of the dielectric loss tangent, tan δ, for $Ca_{9.5-1.5x}MgEu_x(PO_4)_7$ with $x = 0.22$ (1), 0.30 (2), 0.53 (3), 0.72 (4), and 1.00 (5) at 750 kHz. The inset shows the enlargement transition of $x = 0.72$. (b) Dielectric constant ε for the sample with $x = 0.72$.

The temperatures of the ferroelectric phase transitions determined by the dielectric measurements for $Ca_{9.5-1.5x}MgEu_x(PO_4)_7$ phosphates are given in Table 2.

PL/PLE Properties. Figure 7 shows PL spectra recorded under 395 nm excitation. There are several characteristic

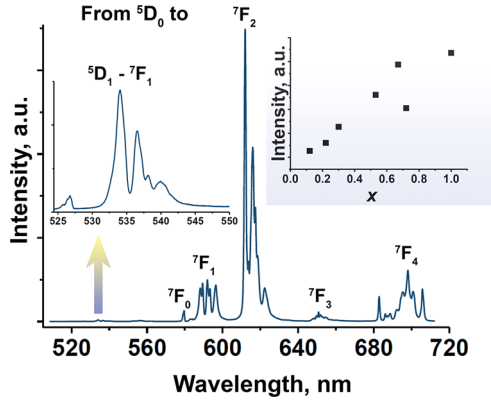

Figure 7. PL spectra for $Ca_{9.5-1.5x}MgEu_x(PO_4)_7$ ($\lambda_{ex} = 395$ nm) at 80 K. The inset shows the dependence of the luminescence intensity on the x Eu^{3+} concentration. $\lambda_{ex} = 395$ nm, and $T = 300$ K.

intraconfigurational f–f transitions from the $^5D_0$ excited state to the ^7F_J ($J = 1-4$) levels of Eu^{3+} ion. Forbidden transitions[41−43] are allowed because of the crystal host symmetry. The broad band typical for Eu^{2+} ion emission[44] was not detected in the PL spectra of the studied samples, confirming the absence of Eu^{2+} in the whole set of solid solutions. The enlargement in Figure 7 shows the PL lines attributed to radiative transitions from the higher level of $^5D_1$. Its low intensity is due to radiative relaxation to $^5D_0$ through a fast phonon-assisted process.[45] The major transition $^5D_0 \rightarrow {}^7F_2$

https://dx.doi.org/10.1021/acs.inorgchem.0c03813
Inorg. Chem. 2021, 60, 3961−3971

at 612 nm corresponds to the red color of the emission. All peaks are well resolved. The measurements at room temperature (300 K) and under cooling (80 K) show the same resolution. A comparison of the spectra at 80 and 300 K is given in Figure S2. The inset in Figure 7 shows the dependence of the luminescence intensity on the Eu^{3+} concentration. The gradual increase of the integral intensity of PL was observed up to $x = 0.67$. However, there was a drop at $x = 0.72$. This fact can be attributed to the rise of polyhedra distortion at the M3 crystal site [DI(M3−O), Table 3]. The full width at half-maximum (fwhm) of the $^5D_0 \rightarrow {}^7F_2$ transition in $Ca_{9.5-1.5x}MgEu_x(PO_4)_7$ differs very slightly from sample to sample and is about 10 nm. This low value meets the requirement of high-performance LED devices.[46]

An interesting feature of the studied samples was the observation of the $^5D_0 \rightarrow {}^7F_5$ transition, which is forbidden by the selection rules and by the Judd−Ofelt theory[41] (Figure S3). This transition (Figure S3, inset) obviously is not observed in most inorganic matrixes.[47,48]

Analysis of the PL spectra at the $^5D_0 \rightarrow {}^7F_0$ transition (Figure 8) reveals splitting and approves the presence of

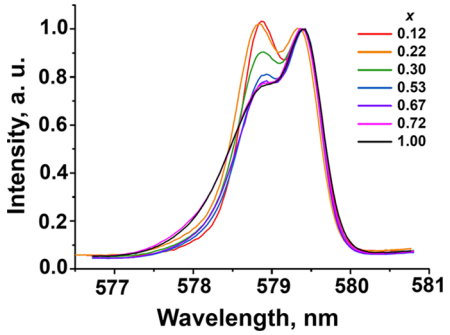

Figure 8. PL spectra for $Ca_{9.5-1.5x}MgEu_x(PO_4)_7$ (λ_{ex} = 395 nm) at the $^5D_0 \rightarrow {}^7F_0$ transition. T = 300 K.

nonequivalent Eu^{3+} positions in the structure. The nonelementary band can be approximated by the sum of three Gaussians with peaks at 579.44 nm (2.140 eV), 578.90 nm (2.142 eV), and 578.36 nm (2.144 eV) (Figure 9). It proves that Eu^{3+} is distributed over three nonequivalent positions. Because the energy position of the $^5D_0 \rightarrow {}^7F_0$ lines is directly related to the mean length of the Eu−O bond,[49] the band at 2.144 eV can be attributed to the M3 site, the band at 2.142 eV to the M1 site, and the band at 2.140 to the M2 site. The intensity of the band related to the M1 site decreases with increasing Eu concentration, while the low-wavelength slope intensity increases. One can suppose that the effect is due to the redistribution of occupancies of the M1 and M3 sites. However, from analysis of the area under the Gaussians and their fwhm values, it follows that there is only a slight variation of the occupancies without a clear tendency (Figure S4). The decrease of the band intensity related to the M1 site is compensated by its broadening, which allows one to keep the area under the curve at approximately the same level. The broadening may be due to distortion of the surroundings (Table 3). Also, this distortion leads to diffusion of the ferroelectric phase transition. The decomposition for all samples is shown in Figure S5.

The relative intensity of the bands in the $^5D_0 \rightarrow {}^7F_0$ transition depends on the excitation wavelength. Under 395 nm excitation, the band at 579.44 nm is the most intensive for

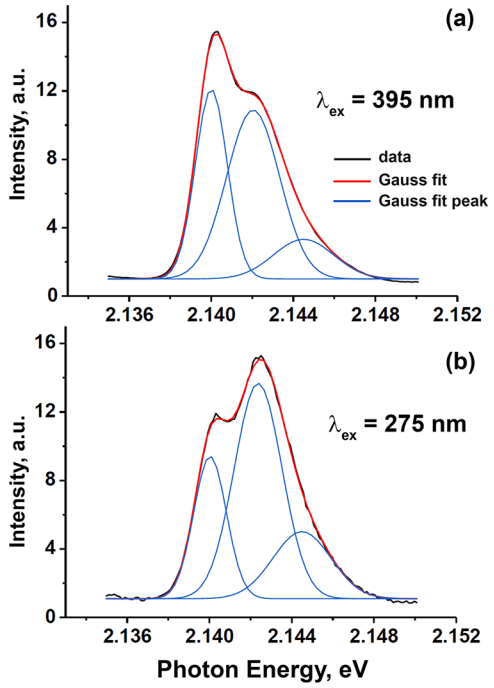

Figure 9. Gauss decomposition of the $^5D_0 \rightarrow {}^7F_0$ transition for $Ca_{9.5-1.5x}MgEu_x(PO_4)_7$ ($x = 0.72$) under 395 nm (a) and 275 nm (b) excitation. T = 300 K.

all samples (Figure 8), except $x = 0.12$ and 0.22. However, under 275 nm excitation, the band at 578.9 nm dominates in the spectra of all samples (Figures 10 and S6). To reveal the differences of excitation of Eu^{3+} in the M1 and M2 sites, the excitation spectra (PLE) for these two bands were measured (Figure 11). The excitation spectrum of Eu^{3+} in the M3 site was not measured because of the low intensity of the corresponding band in the group of $^5D_0 \rightarrow {}^7F_0$ transitions,

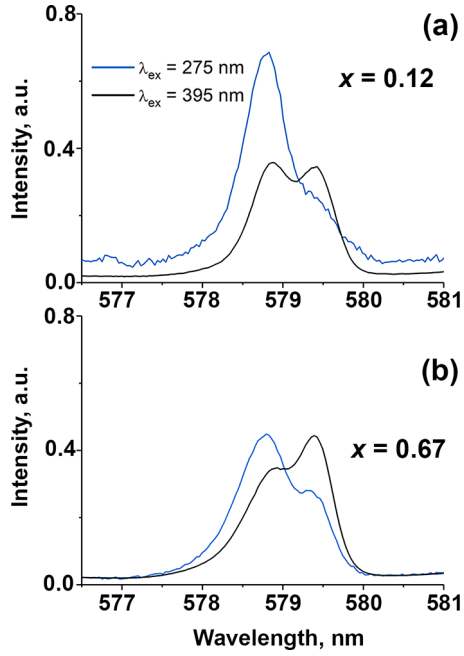

Figure 10. PL spectra for $Ca_{9.5-1.5x}MgEu_x(PO_4)_7$ of $x = 0.12$ (a) and $x = 0.67$ under λ_{ex} = 275 and 395 nm at the $^5D_0 \rightarrow {}^7F_0$ transition. T = 300 K.

https://dx.doi.org/10.1021/acs.inorgchem.0c03813
Inorg. Chem. 2021, 60, 3961−3971

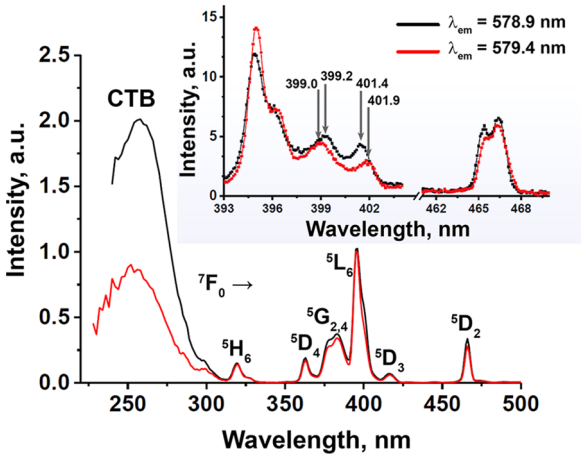

Figure 11. PLE spectra for $Ca_{9.5-1.5x}MgEu_x(PO_4)_7$ of x = 0.53 recorded under λ_{em} = 578.9 and 579.4 nm. The spectra are normalized to the intensity of the peak at 395 nm. The inset shows the resolved structure in the regions of the $^7F_0 \rightarrow {}^5L_6$ and $^7F_0 \rightarrow {}^5D_2$ transitions.

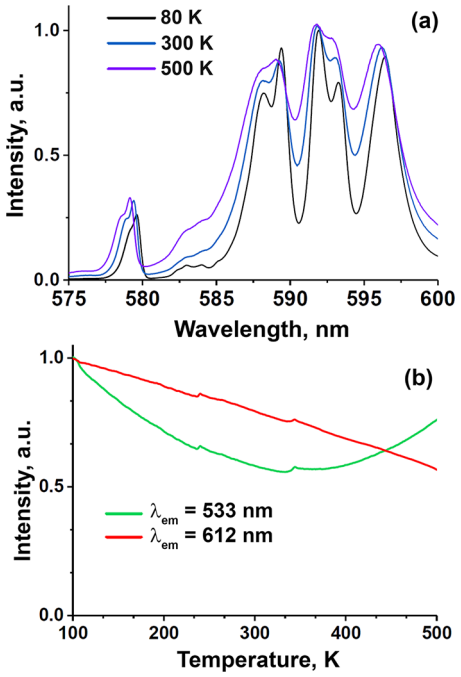

Figure 12. Temperature dependence for $Ca_8MgEu(PO_4)_7$ of (a) the PL spectra at 80, 300, and 500 K (λ_{ex} = 395 nm) and (b) the luminescence intensity of the $^5D_0 \rightarrow {}^7F_2$ and $^5D_1 \rightarrow {}^7F_1$ transitions upon heating. Minor features at 240 and 345 K arise due to the instability of the excitation source.

and it is overlapping with the intensive band connected with Eu^{3+} in M1. The PLE spectra for all samples from the series are shown in Figure S7.

The PLE spectra show broad excitation bands and standard transitions for the Eu^{3+} activator cation (Figure 11). The broad bands from 220 to 320 nm centered at 255 nm are assigned to the charge-transfer band (CTB) and correspond to electrons excited from the 2p delocalized orbital of the O^{2-} ion to the incomplete 4f orbital of the Eu^{3+} ion. In the region from 300 to 500 nm, a series of sharp lines is observed because of the $4f^6-4f^6$ transitions of the Eu^{3+} ion. These bands are attributed to the $^7F_0 \rightarrow {}^5F_2$, $^7F_0 \rightarrow {}^5H_6$, $^7F_0 \rightarrow {}^5D_7$, $^7F_0 \rightarrow {}^5D_4$, $^7F_0 \rightarrow {}^5G_{2,4}$, $^7F_0 \rightarrow {}^5L_6$, $^7F_0 \rightarrow {}^5D_3$, and $^7F_0 \rightarrow {}^5D_2$ transitions at wavelengths of 300, 319, 328, 362, 383, 395, 416, and 464 nm, respectively.

Figure 11 displays changes of the PLE spectrum for the emission bands at 579.44 and 578.90 nm. The energy position of the 4f levels slightly changes for Eu^{3+} occupying different sites, which is revealed by slightly shifted positions of the excitation lines (see the inset in Figure 11). However, the most remarkable difference is the relative intensity of the CTB, which is 2 times higher for λ_{em} = 578.9 nm. This demonstrates that the probability of charge-transfer transitions is strongly dependent on the site symmetry, in which Eu^{3+} is placed. Because CN = 8 in both the M1 and M2 sites, there are eight nonequivalent O atoms in the polyhedra. The DI values for these emitting centers are almost no different. However, the bond length M1−O is greater than M2−O (Table 3). Then, in accordance with the coordinate−configuration model, the nonradiative losses during excitation of the M2 optical center through the CTB are higher than those in the emission of M1; i.e., the energy-transfer efficiency from O 2p to Eu 4f for the optical center M2 will be less (Figure 11).

Figure 12 shows the temperature dependence of the PL spectra. The lines get broader with increasing temperature from 80 to 500 K (Figure 12a), which relates to the higher rate of interaction between the 4f electrons and host matrix phonons. The lower intensity of the emission in the region of $^5D_0 \rightarrow {}^7F_2$ transitions with increasing temperature (Figure 12b) is partially due to thermal quenching of the Eu^{3+} emission and partially due to thermal population of the $^5D_1$ level. The same behavior of the PL spectra was detected for other samples from the series (Figure S8).

However, for the transitions from the $^5D_1$ level, the intensity behavior is different. The intensity decreases up to 335 K and increases for higher temperatures (Figure 12b). The increase relates to thermal population of $^5D_1$ from the lower $^5D_0$ level. Different tendencies in the thermal behavior of the emission lines originating from transitions from the $^5D_1$ and $^5D_0$ levels allow one to consider the studied compounds as phosphors suitable for luminescence thermometry.

CONCLUSIONS

The series of red-emitting phosphors $Ca_{9.5-1.5x}MgEu_x(PO_4)_7$ ($0 \le x \le 1$) with the β-$Ca_3(PO_4)_2$ host structure were synthesized by the standard solid-state route. The structures were studied by PXRD. During the $Ca^{2+} \rightarrow Eu^{3+}$ substitution, it was revealed that $Ca_{9.5-1.5x}MgEu_x(PO_4)_7$ ($0 \le x < 1$) phosphates have a polar structure with SG $R3c$. The presence of three nonequivalent sites of Eu^{3+} was confirmed by luminescence and Mössbauer spectroscopy. Only the limit of a solid solution (x = 1) was classified, as a centrosymmetric sample with SG $R\bar{3}c$. These data were confirmed by dielectric spectroscopy and the SHG method.

On the basis of the Mössbauer spectroscopy data, we obtained the real distribution of Eu^{3+} ions through crystal sites. It was shown that, over the entire range of compositions, Eu^{3+} ions statistically occupy all three large cationic positions M1−M3, wherein the most preferred is the M1 site. This fact is in good agreement with the Rietveld refinement data. Luminescence spectra in the region of $^5D_0-{}^7F_0$ transitions are approximated by the sum of three Gaussians, thus confirming the occupancy of the M1−M3 sites by Eu^{3+}. From luminescent analysis, it follows that the occupancy of the sites by Eu^{3+}

https://dx.doi.org/10.1021/acs.inorgchem.0c03813
Inorg. Chem. 2021, 60, 3961−3971

increases from M3 to M1 and does not considerably change with the Eu^{3+} concentration in accordance with the structure refinement results. The efficiency of excitation via the charge-transfer O 2p−Eu 4f process depends on the polyhedra DI and bond length and is the highest for Eu^{3+} in the M1 site. Thus, the main contribution to the luminescence properties comes from the local state of Eu^{3+} in the M1 site. Radiative transitions from the $^5D_0$ Eu^{3+} excited states decrease with the temperature, which is related to thermal quenching of the emission as well as the thermal population of $^5D_1$ from the lower $^5D_0$ level.

The most intensive sample is $Ca_{8.50}MgEu_{0.67}(PO_4)_7$, which exhibits an exceptionally narrow-band red emission with a maximum at 612 nm and a fwhm of 10 nm, already fulfilling the future standard industrial requirements for high-energy-efficiency phosphor materials for pc-LED applications. The measured QY for $Ca_{9.5-1.5x}MgEu_x(PO_4)_7$ shows excellent results and reaches 63%.

■ ASSOCIATED CONTENT

Supporting Information

The Supporting Information is available free of charge at https://pubs.acs.org/doi/10.1021/acs.inorgchem.0c03813.

Crystallographic data, atomic coordinates and distances, element composition data for $Ca_{9.5-1.5x}MgEu_x(PO_4)_7$, temperature dependence and high-resolution PL and PLE spectra, and Gauss decomposition of the PL spectra for $Ca_{9.5-1.5x}MgEu_x(PO_4)_7$ (PDF)

Accession Codes

CCDC 2052736, 2052846, 2052848,2052849, 2057061, and 2057062 contain the supplementary crystallographic data for this paper. These data can be obtained free of charge via www.ccdc.cam.ac.uk/data_request/cif, or by emailing data_request@ccdc.cam.ac.uk, or by contacting The Cambridge Crystallographic Data Centre, 12 Union Road, Cambridge CB2 1EZ, UK; fax: +44 1223 336033.

■ AUTHOR INFORMATION

Corresponding Author

Dina V. Deyneko − *Department of Chemistry, Lomonosov Moscow State University, Moscow 119991, Russia;* orcid.org/0000-0002-9422-1925; Phone: +74959393687; Email: deynekomsu@gmail.com; Fax: +74959393316

Authors

Dmitry A. Spassky − *Skobeltsyn Institute of Nuclear Physics, Lomonosov Moscow State University, Moscow 119991, Russia; Institute of Physics, University of Tartu, Tartu 50411, Estonia*

Vladimir A. Morozov − *Department of Chemistry, Lomonosov Moscow State University, Moscow 119991, Russia;* orcid.org/0000-0002-0674-2449

Sergey M. Aksenov − *Laboratory of Nature-Inspired Technologies and Environmental Safety of the Arctic, Kola Science Centre, Russian Academy of Sciences, Apatity 184200, Russia;* orcid.org/0000-0003-1709-4798

Stanislav P. Kubrin − *Research Institute of Physics, Southern Federal University, Rostov-on-Don 344090, Russia*

Maxim S. Molokeev − *Laboratory of Crystal Physics, Kirensky Institute of Physics, Federal Research Center, Krasnoyarsk Scientific Center, Siberian Branch of the Russian Academy of Sciences, Krasnoyarsk 660036, Russia; School of Engineering Physics and Radio Electronics, Siberian Federal University, Krasnoyarsk 660041, Russia;* orcid.org/0000-0002-8297-0945

Bogdan I. Lazoryak − *Department of Chemistry, Lomonosov Moscow State University, Moscow 119991, Russia;* orcid.org/0000-0003-1952-5555

Complete contact information is available at: https://pubs.acs.org/10.1021/acs.inorgchem.0c03813

Author Contributions

D.V.D.: writing (original draft), investigation, funding acquisition, and project administration. D.A.S.: writing (review and editing) and investigation. V.A.M.: software and investigation. S.M.A.: writing (review and editing). S.P.K.: investigation. M.S.M.: methodology. B.I.L.: validation.

Notes

The authors declare no competing financial interest.

■ ACKNOWLEDGMENTS

This research was supported by the Russian Science Foundation (Grant 19-77-10013). The authors are grateful to A. V. Morozov (Skolkovo Institute of Science and Technology) for EDX measurements and F. D. Fedyunin for his help with luminescence measurements.

■ REFERENCES

(1) McKittrick, J.; Shea-Rohwer, L. E. Review: Down Conversion Materials for Solid-State Lighting. *J. Am. Ceram. Soc.* **2014**, *97* (5), 1327−1352.

(2) Qiao, J.; Zhao, J.; Liu, Q.; Xia, Z. Recent Advances in Solid-State LED Phosphors with Thermally Stable Luminescence. *J. Rare Earths* **2019**, *37* (6), 565−572.

(3) Smet, P. F.; Parmentier, A. B.; Poelman, D. Selecting Conversion Phosphors for White Light-Emitting Diodes. *J. Electrochem. Soc.* **2011**, *158* (6), R37.

(4) Nardelli, A.; Deuschle, E.; de Azevedo, L. D.; Pessoa, J. L. N.; Ghisi, E. Assessment of Light Emitting Diodes Technology for General Lighting: A Critical Review. *Renewable Sustainable Energy Rev.* **2017**, *75*, 368−379.

(5) Zhao, M.; Zhang, Q.; Xia, Z. Structural Engineering of Eu^{2+} -Doped Silicates Phosphors for LED Applications. *Accounts Mater. Res.* **2020**, *1* (2), 137−145.

(6) Qiao, J.; Zhou, G.; Zhou, Y.; Zhang, Q.; Xia, Z. Divalent Europium-Doped near-Infrared-Emitting Phosphor for Light-Emitting Diodes. *Nat. Commun.* **2019**, *10* (1), 5267.

(7) Cao, Y.; Wang, X.; Ding, J.; Zhou, X.; Seto, T.; Wang, Y. Constructing a Single-White-Light Emission by Finely Modulating the Occupancy of Luminescence Centers in Europium-Doped $(Ca_{1-x}Sr_x)_9Bi(PO_4)_7$ for WLEDs. *J. Mater. Chem. C* **2020**, *8* (28), 9576−9584.

(8) Yu, X.; Yuan, D.; Mi, X. Hydrothermal Synthesis and Luminescent Properties of $Ca_3(PO_4)_2$:Dy^{3+} White-Emitting Phosphors. *J. Alloys Compd.* **2021**, *857*, 157585.

(9) Liu, S.; Liang, Y.; Li, H.; Zhang, W.; Tu, D.; Chen, Y. Color Tuning of β- $Ca_3(PO_4)_2$-Type Phosphor with Enhanced Quantum Efficiency via Self-Charge Compensation for Healthy and Warm Solid State Lighting Application. *Chem. Eng. J.* **2020**, *390*, 124463.

(10) Luo, J.; Sun, Z.; Zhu, Z.; Zhang, X.; Wu, Z.; Mo, F. Synthesis, Structure and Luminescence of a High-Purity and Thermal-Stable $Sr_9LiMg(PO_4)_7$:Eu^{3+} Red Phosphor. *Ceram. Int.* **2020**, *46* (8), 11994−12000.

(11) Wang, S.; Han, Y.; Lu, X.-L.; Guo, Y.; Wang, Z.; Zhang, B.; Mu, Z.; Shen, S.; Zhang, Z.; Song, A. A Dual-Emission $Ca_9MgLi(PO_4)_7$:Ce^{3+}, Mn^{2+} Phosphor with Energy Transfer for Plant-Lighting. *Opt. Mater. (Amsterdam, Neth.)* **2020**, *108*, 110201.

(12) Wang, J.; Su, R.; Cui, M.; Shang, M. Tunable Emission Properties of Tri-Doped $Ca_9LiY_{2/3}(PO_4)_7$:Ce^{3+},Tb^{3+},Mn^{2+} Phosphors with Warm White Emitting Based on Energy Transfer. *J. Rare Earths* **2020**, DOI: 10.1016/j.jre.2020.05.001.
(13) Chen, M.; Xia, Z.; Molokeev, M. S.; Lin, C. C.; Su, C.; Chuang, Y.-C.; Liu, Q. Probing Eu^{2+} Luminescence from Different Crystallographic Sites in $Ca_{10}M(PO_4)_7$:Eu^{2+} (M = Li, Na, and K) with β-$Ca_3(PO_4)_2$-Type Structure. *Chem. Mater.* **2017**, *29* (17), 7563−7570.
(14) Yashima, M.; Sakai, A.; Kamiyama, T.; Hoshikawa, A. Crystal Structure Analysis of β-Tricalcium Phosphate $Ca_3(PO_4)_2$ by Neutron Powder Diffraction. *J. Solid State Chem.* **2003**, *175*, 272.
(15) Tanner, P. A. Some Misconceptions Concerning the Electronic Spectra of Tri-Positive Europium and Cerium. *Chem. Soc. Rev.* **2013**, *42* (12), 5090.
(16) U.S. Department of Energy. Solid state lighting research and development plan. https://energy.gov/sites/prod/files/2016/06/f32/ssl_rd-plan_%25%0A20jun2016_2.pdf.
(17) Ofelt, G. S. Structure of the f^6 Configuration with Application to Rare-Earth Ions. *J. Chem. Phys.* **1963**, *38* (9), 2171−2180.
(18) Judd, B. R. Hypersensitive Transitions in Rare-Earth Ions. *J. Chem. Phys.* **1966**, *44* (2), 839−840.
(19) Belik, A. A.; Morozov, V. A.; Deyneko, D. V.; Savon, A. E.; Baryshnikova, O. V.; Zhukovskaya, E. S.; Dorbakov, N. G.; Katsuya, Y.; Tanaka, M.; Stefanovich, S. Y.; Hadermann, J.; Lazoryak, B. I. Antiferroelectric Properties and Site Occupations of R^{3+} Cations in $Ca_8MgR(PO_4)_7$ Luminescent Host Materials. *J. Alloys Compd.* **2017**, *699*, 928−937.
(20) Petricek, V.; Dusek, M.; Palatinus, L. Crystallographic Computing System JANA2006: General FEATures. *Z. Kristallogr. - Cryst. Mater.* **2014**, *229*, 345−352.
(21) Brandenburg, K. *DIAMOND*, version 2.1c; Crystal Impact 627 GbR: Bonn, Germany, 1999.
(22) Deyneko, D. V.; Morozov, V. A.; Hadermann, J.; Savon, A. E.; Spassky, D. A.; Stefanovich, S. Y.; Belik, A. A.; Lazoryak, B. I. A Novel Red $Ca_{8.5}Pb_{0.5}Eu(PO_4)_7$ Phosphor for Light Emitting Diodes Application. *J. Alloys Compd.* **2015**, *647*, 965−972.
(23) Ruan, F.; Deng, D.; Wu, M.; Chen, B.; Lei, L.; Lei, R.; Xu, S. Multichannel Luminescence Properties and Ultrahigh-Sensitive Optical Temperature Sensing of Mixed-Valent Eu^{2+}/Eu^{3+} Co-Activated $Ca_8ZrMg(PO_4)_6(SiO_4)$ Phosphors. *J. Alloys Compd.* **2019**, *784*, 1153−1161.
(24) Shannon, R. D. Revised Effective Ionic Radii and Systematic Studies of Interatomic Distances in Halides and Chalcogenides. *Acta Crystallogr., Sect. A: Cryst. Phys., Diffr., Theor. Gen. Crystallogr.* **1976**, *32* (5), 751−767.
(25) Xie, M. Structure, Site Occupancies, and Luminescence Properties of $Ca_{10}M(PO_4)_7$:Ce^{3+} (M = Li, Na, K) Phosphors. *J. Alloys Compd.* **2019**, *775*, 1129−1135.
(26) Golim, O. P.; Huang, S.; Yin, L.; Yang, T.; Zhou, H.; Gao, W.; Söhnel, T.; Cao, P. Synthesis, Neutron Diffraction and Photoluminescence Properties of a Whitlockite Structured $Ca_9MgLi(PO_4)_7$:Pr^{3+} Phosphor. *Ceram. Int.* **2020**, *46* (17), 27476−27483.
(27) Xie, M.; Wang, J.; Ruan, W. Multi-Site Tunable Emission of Eu^{2+} Ions in $Ca_{10}Na(PO_4)_7$ Host. *J. Lumin.* **2020**, *218*, 116848.
(28) Wang, S.; Han, Y.; Shi, L.; Tong, Y.; Zhao, Q.; Zhang, J.; Mao, Z.; Mu, Z.; Zhang, Z.; Niu, S. A New Strategy to the Phosphors for Plant Growth LEDs: Far Red Emission from the $Ca_9MY_{0.667}(PO_4)_7$ (M = Li, Na):Eu^{3+} Phosphors Due to the Eu^{3+}: $^5D_0 \rightarrow {}^7F_4$ Transition. *J. Lumin.* **2020**, *225*, 117404.
(29) Xie, F.; Xu, D.; Wu, Z.; Molokeev, M. S.; Milićević, B.; Li, H.; Shi, J. Improving Thermal Stability of Novel Single-Component White-Light Emitting Phosphor $Ca_8MgLu(PO_4)_7$:Tm^{3+}, Dy^{3+} by Back-Energy-Transfer. *J. Lumin.* **2020**, *227*, 117516.
(30) Li, L.; Dou, M.; Yan, Y.; Li, Y.; Ling, F.; Jiang, S.; Xiang, G.; Liu, J.; Zhou, X. Insight into Energy Transfer, Color Tuning, and White Emission in Tm^{3+} and Dy^{3+} Codoped $Ca_8ZnLa(PO_4)_7$ Phosphors. *Opt. Mater. (Amsterdam, Neth.)* **2020**, *102*, 109808.
(31) Dikhtyar, Y. Y.; Deyneko, D. V.; Spassky, D. A.; Lazoryak, B. I.; Stefanovich, S. Y. A Novel High Color Purity Blue-Emitting Tm^{3+}-Doped β-$Ca_3(PO_4)_2$-Type Phosphor for WLED Application. *Optik (Munich, Ger.)* **2021**, *227*, 166027.
(32) Nikiforov, I. V.; Deyneko, D. V.; Spassky, D. A.; Baryshnikova, O. V.; Stefanovich, S. Y.; Lazoryak, B. I. Tunable Luminescence and Energy Transfer in Eu^{3+} Doped $Ca_8MTb(PO_4)_7$ (M = Mg, Zn, Ca) Phosphors. *Mater. Res. Bull.* **2020**, *130*, 110925.
(33) Deyneko, D. V.; Morozov, V. A.; Zhukovskaya, E. S.; Nikiforov, I. V.; Spassky, D. A.; Belik, A. A.; Lazoryak, B. I. The Influence of Second Coordination-Sphere Interactions on the Luminescent Properties of β-$Ca_3(PO_4)_2$-Related Compounds. *J. Alloys Compd.* **2020**, *815*, 152352.
(34) Wu, H.; Li, H.; Jiang, L.; Pang, R.; Zhang, S.; Li, D.; Liu, G.; Li, C.; Feng, J.; Zhang, H. Synthesis, Structure and Optical Properties of Novel Thermally Robust Dy^{3+}-Doped $Ca_9Sc(PO_4)_7$ Phosphors for NUV-Excited White LEDs. *J. Rare Earths* **2021**, *39*, 277−283.
(35) Han, Y.; Wang, S.; Liu, H.; Shi, L.; Liu, S.; Zhang, Y.; Liu, C.; Shi, X.; Wang, Q.; Mu, Z.; Mao, Z.; Wang, D.; Zhang, Z. A Novel Promising Red Phosphor $Ca_9LiBi_{0.667}(PO_4)_7$:Eu^{3+} with Excellent Responsiveness to Phytochrome PFR for the Indoor Plant Cultivation. *J. Mol. Struct.* **2020**, *1210*, 127998.
(36) Liu, S.; Liang, Y.; Zhu, Y.; Li, H.; Chen, J.; Wang, S. The Exploration of Structure Evolution and Photoluminescence Property in $Ca_9Al_{1-Y}(PO_4)_7$:Eu^{2+} Solid Solution Phosphors via the Construction of Bi-Directional Relationships. *J. Alloys Compd.* **2019**, *785*, 573−583.
(37) Dickens, B.; Schroeder, L. W.; Brown, W. E. Crystallographic Studies of the Role of Mg as a Stabilizing Impurity in β-$Ca_3(PO_4)_2$. The Crystal Structure of Pure β- $Ca_3(PO_4)_2$. *J. Solid State Chem.* **1974**, *10* (3), 232−248.
(38) Beskorovaynaya, D. A.; Deyneko, D. V.; Baryshnikova, O. V.; Stefanovich, S. Y.; Lazoryak, B. I. Optical Non-Linearity Tuning in $Ca_{8-x}PbMBi(VO_4)_7$ Whitlockite-Type Systems. *J. Alloys Compd.* **2016**, *674*, 323−330.
(39) Lazoryak, B. I.; Zhukovskaya, E. S.; Baryshnikova, O. V.; Belik, A. A.; Leonidova, O. N.; Deyneko, D. V.; Savon, A. E.; Dorbakov, N. G.; Morozov, V. A. Luminescence, Structure and Antiferroelectric-Type Phase Transition in $Ca_8ZnEu(PO_4)_7$. *Mater. Res. Bull.* **2018**, *104*, 20−26.
(40) Deyneko, D. V.; Petrova, D. A.; Aksenov, S. M.; Stefanovich, S. Y.; Baryshnikova, O. V.; Fedotov, S. S.; Burns, P. C.; Kosmyna, M. B.; Shekhovtsov, A. N.; Lazoryak, B. I. Ferroelectricity, Ionic Conductivity and Structural Paths for Large Cation Migration in $Ca_{10.5-x}Pb_x(VO_4)_7$ Single Crystals, x = 1.9, 3.5, 4.9. *CrystEngComm* **2019**, *21* (8), 1309.
(41) Judd, B. R. Optical Absorption Intensities of Rare-Earth Ions. *Phys. Rev.* **1962**, *127* (3), 750−761.
(42) Ofelt, G. S. Intensities of Crystal Spectra of Rare-Earth Ions. *J. Chem. Phys.* **1962**, *37* (3), 511−520.
(43) Porcher, P.; Caro, P. Influence of J-Mixing on the Phenomenological Interpretation of the Eu^{3+} Ion Spectroscopic Properties. *J. Lumin.* **1980**, *21* (2), 207−216.
(44) Qiao, J.; Zhao, J.; Xia, Z. (INVITED) A Review on the Eu^{2+} Doped β- $Ca_3(PO_4)_2$-Type Phosphors and the Sites Occupancy for Photoluminescence Tuning. *Opt. Mater. X* **2019**, *1*, 100019.
(45) Berdowski, P. A. M.; Blasse, G. Non-Radiative Relaxation of the Eu^{3+} $^5D_1$ Level in $NaGdTiO_4$. *Chem. Phys. Lett.* **1984**, *107* (3), 351−354.
(46) Hoerder, G. J.; Seibald, M.; Baumann, D.; Schröder, T.; Peschke, S.; Schmid, P. C.; Tyborski, T.; Pust, P.; Stoll, I.; Bergler, M.; Patzig, C.; Reißaus, S.; Krause, M.; Berthold, L.; Höche, T.; Johrendt, D.; Huppertz, H. $Sr[Li_2Al_2O_2N_2]$:Eu^{2+}—A High Performance Red Phosphor to Brighten the Future. *Nat. Commun.* **2019**, *10* (1), 1824.
(47) Binnemans, K. Interpretation of Europium(III) Spectra. *Coord. Chem. Rev.* **2015**, *295*, 1−45.
(48) Tuan, D. C.; Olazcuaga, R.; Guillen, F.; Garcia, A.; Moine, B.; Fouassier, C. Luminescent Properties of Eu^{3+} -Doped Yttrium or Gadolinium Phosphates. *J. Phys. IV* **2005**, *123*, 259−263.
(49) Benhamou, R. A.; Bessière, A.; Wallez, G.; Viana, B.; Elaatmani, M.; Daoud, M.; Zegzouti, A. New Insight in the Structure-

Luminescence Relationships of $Ca_9Eu(PO_4)_7$. *J. Solid State Chem.* **2009**, *182* (8), 2319−2325.

https://dx.doi.org/10.1021/acs.inorgchem.0c03813
Inorg. Chem. 2021, 60, 3961−3971